RSC Advances

PAPER

View Article Online
View Journal | View Issue

Cite this: *RSC Adv.*, 2018, **8**, 30087

Urea-assisted hydrothermal synthesis of a hollow hierarchical $LiNi_{0.5}Mn_{1.5}O_4$ cathode material with tunable morphology characteristics†

Xing Qin,[abc] Mushang Zhou,[abc] Bo Zong,[abc] Jianling Guo,[abc] Jiajia Gong,[abc] Li Wang *[abc] and Guangchuan Liang [abc]

Received 8th July 2018
Accepted 19th August 2018

DOI: 10.1039/c8ra05817b

rsc.li/rsc-advances

A hollow hierarchical $LiNi_{0.5}Mn_{1.5}O_4$ cathode material has been synthesized *via* a urea-assisted hydrothermal method followed by a high-temperature calcination process. The effect of reactant concentration on the structure, morphology and electrochemical properties of the carbonate precursor and corresponding $LiNi_{0.5}Mn_{1.5}O_4$ product has been intensively investigated. The as-prepared samples were characterized by XRD, FT-IR, SEM, CV, EIS, GITT and constant-current charge/discharge tests. The results show that all samples belong to a cubic spinel structure with mainly *Fd*3*m* space group, and the Mn^{3+} content and impurity content initially decrease and then increase slightly with the reactant concentration increasing. SEM observation shows that the particle morphology and size of carbonate precursor can be tailored by changing reactant concentration. The $LiNi_{0.5}Mn_{1.5}O_4$ sample obtained from the carbonate precursor hydrothermally synthesized at a reactant concentration of 0.3 mol L^{-1} exhibits the optimal overall electrochemical properties, with capacity retention rate of 96.8% after 100 cycles at 1C rate and 10C discharge capacity of 124.9 mA h g^{-1}, accounting for 99.9% of that at 0.2C rate. The excellent electrochemical performance can be mainly attributed to morphological characteristics, that is, smaller particle size with homogeneous distribution, in spite of lower Mn^{3+} content.

Introduction

Lithium ion batteries (LIBs) are being intensively pursued for high-power and high-energy applications such as electric vehicles (EVs) and hybrid electric vehicles (HEVs).[1,2] The energy density of LIB is generally limited by the cathode material. One practical and cost-effective way to improve the energy density of cathode material is elevating the working voltage. Among all cathode materials, $LiNi_{0.5}Mn_{1.5}O_4$ spinel has been regarded as one of the most promising cathodes for LIB, owing to high working voltage (4.7 V *vs.* Li/Li^+) and high energy density (650 W h kg^{-1}).[3,4] In addition, the inherently fast Li^+ ion diffusion within its 3D spinel structure leads to good rate capability and cycling stability.[5] However, simultaneously achieving satisfactory cyclability and rate performance for $LiNi_{0.5}Mn_{1.5}O_4$ remains challenging due to complex performance-influencing factors and electrolyte/structure instability under high potential.[6,7]

To date, there are three main approaches to solve the above problem, such as surface modification, cation doping and particle size reduction to nanoscale level. The nanosized materials generally show improved rate performance by shorter Li^+ ion diffusion channel and larger surface area. Unfortunately, low thermodynamic stability of nanoparticles results in electrochemical agglomeration and raises the risk of side reaction with electrolyte, thus leading to inferior cycling stability.[8,9] Recently, the cathodes with hierarchical hollow structure have attracted considerable interests for the co-improvement of rate capability and cycle performance.[10,11] On the one hand, this kind of structure can provide a shorter path for Li^+ ion diffusion and meanwhile have larger electrode/electrolyte contact area for Li^+ flux across the interface, resulting in better rate capability. On the other hand, the hollow interior can improve the structural integrity by alleviating the mechanical strain induced by volume change during the repeated Li^+ ion insertion/extraction processes, which can promote the cycling stability.[5,10,12–16]

At present, the $LiNi_{0.5}Mn_{1.5}O_4$ cathode material with hollow hierarchical structure has been generally synthesized by high-temperature calcination using $MnCO_3$,[11,15,17] manganese oxides converted from $MnCO_3$,[5,10,18] or $Ni_{0.25}Mn_{0.75}CO_3$ (ref. 19–21) as self-template and Mn/Ni source. In the above

[a]*Institute of Power Source and Ecomaterials Science, Hebei University of Technology, Tianjin 300130, China. E-mail: wangli_hebut@163.com*

[b]*Key Laboratory of Special Functional Materials for Ecological Environment and Information (Hebei University of Technology), Ministry of Education, Tianjin 300130, China*

[c]*Key Laboratory for New Type of Functional Materials in Hebei Province, Hebei University of Technology, Tianjin 300130, China*

† Electronic supplementary information (ESI) available. See DOI: 10.1039/c8ra05817b

literatures, most of $MnCO_3$ or $Ni_{0.25}Mn_{0.75}CO_3$ has been synthesized by direct precipitation method between NH_4HCO_3/Na_2CO_3 precipitant and Mn/Ni salt solution, which may lead to the inhomogeneous particle size distribution of as-prepared carbonate precursor and corresponding $LiNi_{0.5}Mn_{1.5}O_4$ product. To address above-mentioned problem, in this work, the Ni–Mn carbonate precursor was initially synthesized *via* a homogenous precipitation-hydrothermal method using urea as a precipitant reservoir, and $LiNi_{0.5}Mn_{1.5}O_4$ cathode material with hollow hierarchical structure was achieved by high-temperature calcination process with lithium source. As is well known, the key point to fabricate hierarchical material is control of the precursor. During the hydrothermal process, the urea is slowly decomposed to generate precipitating agent (CO_3^{2-}) in the reaction mixture, allowing particle ripening during precipitation and often resulting in better crystallinity, regular shape and size of particles.[8] There are many influencing factors during the hydrothermal process, such as hydrothermal temperature, hydrothermal duration, molar ratio of urea to transition metal ions, solvent, reactant concentration, *etc.* The hydrothermal temperature, hydrothermal duration, molar ratio of urea to transition metal ions and solvent have been investigated in our previous work, which have been determined as 180 °C, 10 h, 2 : 1, mixed solvent of H_2O and ethylene glycol (v/v = 6 : 1), respectively. Although there are many reports on the urea-assisted hydrothermal method,[22–28] the effect of reactant concentration on the structure, morphology and electrochemical properties of carbonate precursor and corresponding product was rarely involved, which was just the focus of this work. It has been found that the reactant concentration exerts great influence on the particle morphology and size of carbonate precursors, thus resulting in different electrochemical properties of corresponding $LiNi_{0.5}Mn_{1.5}O_4$ products.

Experimental

Sample synthesis

Firstly, the carbonate precursor was synthesized by a urea-assisted hydrothermal method. The specific preparation process was just as follows. $Ni(CH_3COO)_2 \cdot 4H_2O$, $Mn(CH_3COO)_2 \cdot 4H_2O$ and urea were dissolved in 75 mL of a mixture of deionized water and EG (6 : 1, v/v) under stirring, then transferred to a 100 mL Teflon-lined stainless-steel autoclave and heated at 180 °C for 10 h. The total molar concentration of transition metal ions (reactant concentration) was selected as 0.1, 0.2, 0.3 and 0.4 mol L^{-1}, respectively. The molar ratio of urea to transition metal ions was set as 2 : 1. After cooling to room temperature naturally, the resulting carbonate precursor was centrifuged, and washed with water and ethanol several times. The dried carbonate precursor and stoichiometric amount of Li_2CO_3 (5% excess to make up for the lithium volatilization during calcination) were dispersed in ethanol, and the ethanol was evaporated slowly at room temperature under continuous stirring. Finally, the mixture was calcined at 750 °C for 12 h in the air to obtain the $LiNi_{0.5}Mn_{1.5}O_4$ product. The carbonate precursors synthesized at reactant concentrations of 0.1, 0.2, 0.3, 0.4 mol L^{-1} were labelled as NMC-0.1, NMC-0.2, NMC-0.3, NMC-0.4, and the resulting $LiNi_{0.5}Mn_{1.5}O_4$ products were named as LNMO-0.1, LNMO-0.2, LNMO-0.3, LNMO-0.4, respectively.

Sample characterization

XRD and FT-IR were performed to analyse the structural properties of as-synthesized carbonate precursor and $LiNi_{0.5}Mn_{1.5}O_4$ powders by Bruker D8-FOCUS X-ray diffractometer (CuKα radiation) and Bruker V80 Fourier Transformation Infrared Spectrometer, respectively. SEM was performed to observe the particle morphology and size on a FEI Nova Nano SEM450 instrument. Brunauer–Emmett–Teller (BET) analysis of the sample was measured with an ASAP 2460 surface area and pore size analyser. The pore size distribution was calculated by the Barrett–Joyner–Halenda (BJH) method using nitrogen adsorption data.

The Ni/Mn content in $LiNi_{0.5}Mn_{1.5}O_4$ product was measured by a chemical titration method, and the residual Ni^{2+} content in the filtrate was measured by a spectrophotometer (T6, PERSEE, Beijing). The detailed procedures are illustrated in ESI.†

Electrochemical measurements

The electrochemical measurements were carried out using CR2032 coin cells. Test electrodes were prepared as follows: 80 wt% as-prepared $LiNi_{0.5}Mn_{1.5}O_4$ powder, 15 wt% ethylene black and 5 wt% PTFE were mixed in alcohol and then ultrasonically dispersed uniformly to form a slurry. After the evaporation of alcohol, the mixture was rolled to a thin film with a thickness of 0.14 mm. The round electrode plate with a diameter of 12 mm and active material loading of ~10 mg was cut down for coin assembly. The Li metal, Celgard 2400 and a solution of 1 M $LiPF_6$ in EC : DMC : EMC (1 : 1 : 1 in volume) were used as the counter electrode, separator and electrolyte, respectively. The coin cells were assembled in an argon-filled glove box. For rate capability tests, the cells were charged and discharged between 3.5 and 4.95 V (*vs.* Li/Li^+) at 0.2C, 1C, 5C and 10C rates. For cycling experiments, the cells were charged and discharged at 1C rate. The electrochemical measurement was carried out using Land battery measurement system (Wuhan, China) at room temperature. In order to calculate the lithium ion diffusion coefficient during charge/discharge process, galvanostatic intermittent titration technique (GITT) was also performed on this apparatus at 0.1C. The cell was charged/discharged for 10 min and then followed by a relaxation time of 30 min between 3.5 and 4.95 V during the 3rd change/discharge process after two activation cycles at 0.2C rate. The electrochemical impedance spectroscopy (EIS) was measured using an electrochemical workstation (CHI660D) in the frequency range of 100 kHz to 10 mHz with an AC amplitude of 5 mV at full-discharged state after cycling 3 times at 1C rate. The cyclic voltammetry (CV) was measured from 3.4 to 5.0 V at scan rate of 0.1 mV s^{-1}.

Results and discussion

Structure of samples

Fig. 1(a) shows the XRD patterns of carbonate precursors synthesized at different reactant concentrations. It can be seen that the diffraction patterns of all four precursors can be indexed to a typical carbonate structure based on $MnCO_3$ (JCPDS card no.: 44-1472) and $NiCO_3$ (JCPDS card no.: 12-0771). It is inferred that the precursors synthesized at different reactant concentrations consist of both $MnCO_3$ and $NiCO_3$ phases. The diffraction peak becomes gradually broadened with the increase of reactant concentration, implying a gradual decrease in crystal size, which can be verified by the following SEM observation in Fig. 3. In addition, the peak intensity of $NiCO_3$ is gradually decreased with the reactant concentration, implying the gradually incomplete precipitation of $NiCO_3$ ($K_{sp} = 1.42 \times 10^{-7}$, 25 °C) due to its higher solubility product than $MnCO_3$ ($K_{sp} = 2.24 \times 10^{-11}$, 25 °C) and higher complex equilibrium constant of $[Ni(NH_3)_n]^{2+}$ ($\lg K_f = 8.12$ for $n = 4$) than $[Mn(NH_3)_n]^{2+}$ ($\lg K_f = 1.3$ for $n = 4$).[29] This can be verified by the remaining Ni^{2+} contents in the filtrate measured by spectrophotometry method, which are 7.14, 35.45, 63.32 and 105.36 mg L^{-1}, respectively, for NMC-0.1, NMC-0.2, NMC-0.3 and NMC-0.4 samples. The contents of Ni and Mn in $LiNi_{0.5}Mn_{1.5}O_4$ product were measured *via* the chemical titration method as illustrated in ESI.† The obtained molar ratios of Ni and Mn are 0.495 : 1.5, 0.490 : 1.5, 0.485 : 1.5 and 0.479 : 1.5, respectively, for LNMO-0.1, LNMO-0.2, LNMO-0.3 and LNMO-0.4 samples, in consistence with the residual Ni^{2+} concentrations in the filtrate. It can be seen that all four samples show different levels of nickel deficiency compared to the stoichiometric $LiNi_{0.5}Mn_{1.5}O_4$, and the nickel deficiency becomes gradually more severe with the reactant concentration.

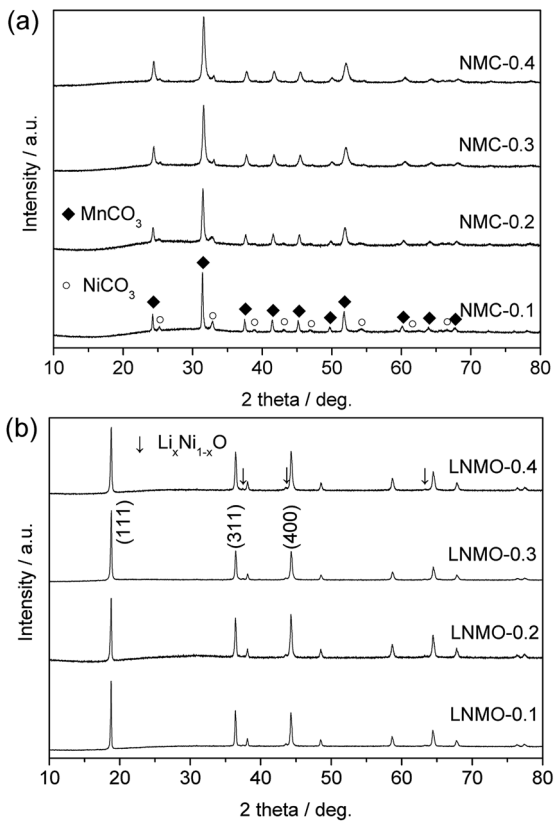

Fig. 1 XRD patterns of carbonate precursors (a) and $LiNi_{0.5}Mn_{1.5}O_4$ samples (b) synthesized at different reactant concentrations.

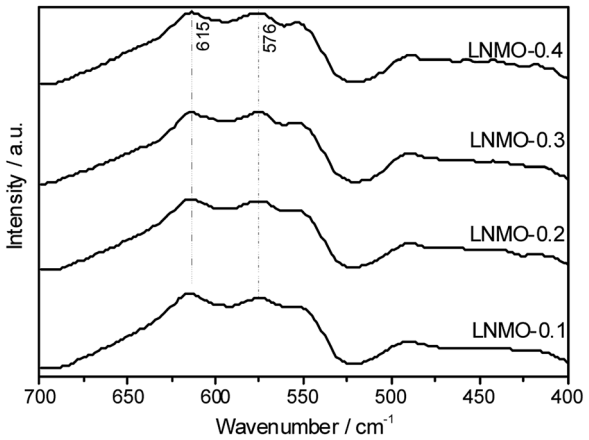

Fig. 2 FT-IR spectra of $LiNi_{0.5}Mn_{1.5}O_4$ samples synthesized at different reactant concentrations.

Fig. 1(b) shows the XRD patterns of $LiNi_{0.5}Mn_{1.5}O_4$ samples synthesized at different reactant concentrations. It can be seen that all four patterns can be assigned to cubic spinel $LiNi_{0.5}Mn_{1.5}O_4$ (JCPDS card no.: 80-2162). Some weak peaks at $2\theta =$ 37.5, 43.6 and 63.4° (marked with arrow) can be ascribed to a rock-salt impurity phase ($Li_xNi_{1-x}O$, and/or Ni_6MnO_8),[30,31] which can be clearly seen in local enlarged image between 35° and 45° in Fig. S1.† The content of impurity phase can be roughly estimated by calculating the ratio of peak intensity at $2\theta = 43.6°$ of impurity phase to that at $2\theta = 44.3°$ of spinel phase.[32] The intensity ratios are 3.62 : 100, 3.20 : 100, 2.96 : 100 and 3.36 : 100, respectively, for LNMO-0.1, LNMO-0.2, LNMO-0.3 and LNMO-0.4 samples, that is, the impurity content decreases in the order of LNMO-0.1 > LNMO-0.4 > LNMO-0.2 > LNMO-0.3. Among them, the $LiNi_{0.5}Mn_{1.5}O_4$ sample synthesized at reactant concentration of 0.3 mol L^{-1} has the lowest impurity content, which is believed to be advantageous to electrochemical property, because it is recognized that the presence of rock-salt impurity phase may lower discharge capacity and block Li^+ mobility in the material.[33] What's more, the variation rule of impurity phase content is the same as that of Mn^{3+} content, so the reason will be given in the following discussion of Mn^{3+} content.

Table 1 lists the lattice parameters of four samples obtained from the Rietveld refinement results, as shown in Fig. S2,† based on *Fd3m* space group. From the refinement factors listed in Table S1,† it can be clearly seen that the refinement yields good agreement factors, with R_{wp} values less than 10% and GOF values between 1 and 2, suggesting an acceptable refinement. As shown in Table 1, the lattice parameter a is 8.1708, 8.1688, 8.1666 and 8.1669 Å for LNMO-0.1, LNMO-0.2, LNMO-0.3 and LNMO-0.4 samples, respectively. It can be seen that the lattice parameter initially decreases and then increases slightly with

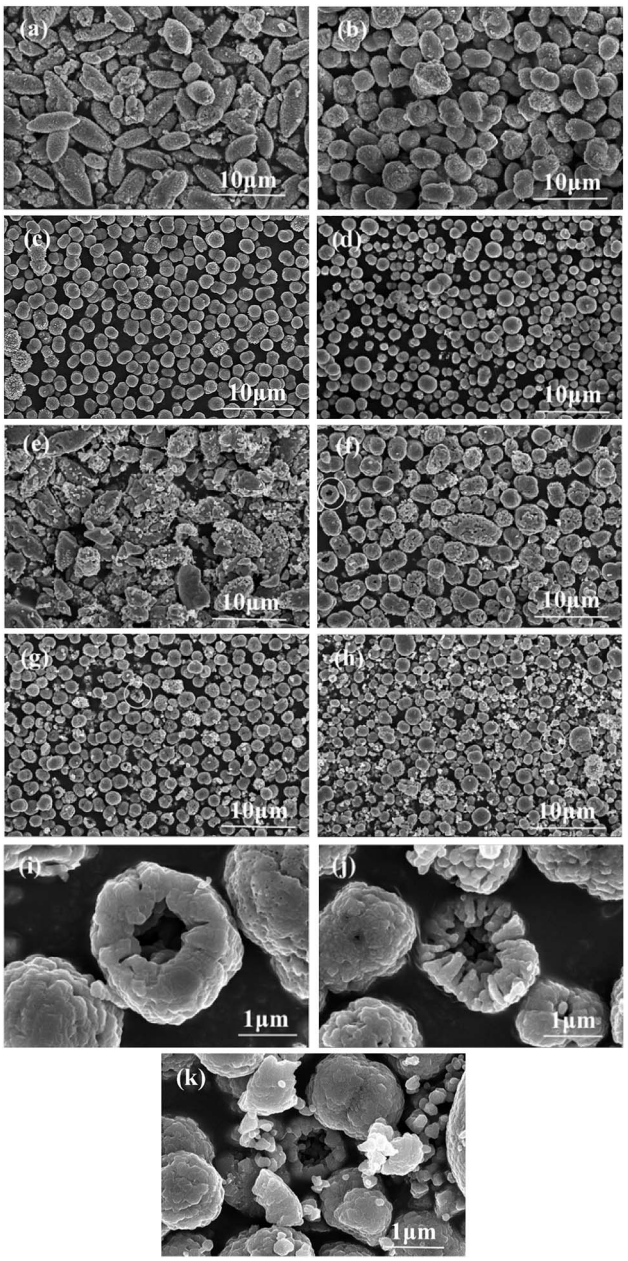

Fig. 3 SEM images of carbonate precursor (a–d) and $LiNi_{0.5}Mn_{1.5}O_4$ samples (e–k) (a and e) 0.1 mol L^{-1}, (b, f and i) 0.2 mol L^{-1}, (c, g and j) 0.3 mol L^{-1}, (d, h and k) 0.4 mol L^{-1}.

Table 1 Lattice parameters and I_{311}/I_{400} ratios of $LiNi_{0.5}Mn_{1.5}O_4$ samples synthesized at different reactant concentrations

Sample	a (Å)	V (Å^3)	I_{311}/I_{400}
LNMO-0.1	8.1708	545.51	1.038
LNMO-0.2	8.1688	545.09	0.880
LNMO-0.3	8.1666	544.67	0.991
LNMO-0.4	8.1669	544.72	0.942

the reactant concentration increasing, which may be caused by the variation of Mn^{3+} content, as Mn^{3+} (0.645 Å) has a larger ionic radius than Mn^{4+} (0.53 Å). The variation of Mn^{3+} content is

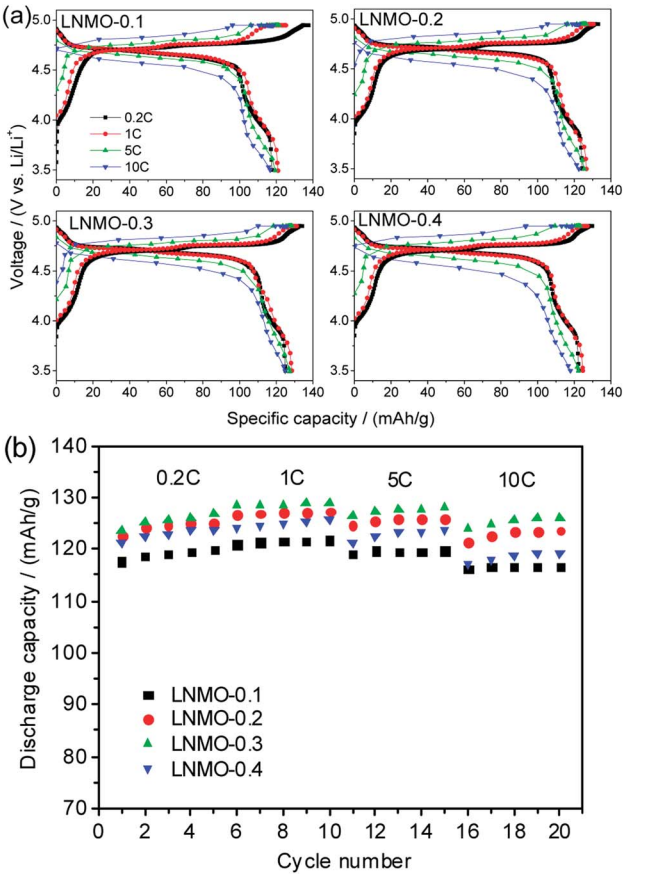

Fig. 4 Charge/discharge curves at various rates (a) and rate capability curves (b) for $LiNi_{0.5}Mn_{1.5}O_4$ samples synthesized at different reactant concentrations.

reported to be closely related to the particle size. Xue *et al.*[32] found that under the same calcination condition, the different Mn^{3+} content in spinel sample could be ascribed to an inhomogeneous migration of atoms. During calcination process, Ni and Mn atoms have to migrate a distance to form a homogeneous $LiNi_{0.5}Mn_{1.5}O_4$ phase. The shorter the distance, the more uniform the diffusion. The smaller particle size means shorter migration distance of atoms, thus leading to more homogeneous Ni/Mn distribution and lower Mn^{3+} content. Due to the smaller particle size and more homogeneous distribution, LNMO-0.3 sample exhibits the lowest Mn^{3+} content. As for LNMO-0.4 sample, the slightly higher Mn^{3+} content may be ascribed to the existence of some larger agglomerate particles.

For spinel $LiMn_2O_4$, the I_{311}/I_{400} peak intensity ratio can reflect the degree of tetragonal distortion from cubic spinel structure.[34] Therefore, the I_{311}/I_{400} ratio can also reflect the structural integrity of $LiNi_{0.5}Mn_{1.5}O_4$ spinel structure.[35,36] The smaller the I_{311}/I_{400} ratio, the better the structural stability. As shown in Table 1, the I_{311}/I_{400} ratios are 1.038, 0.880, 0.991 and 0.942 for LNMO-0.1, LNMO-0.2, LNMO-0.3 and LNMO-0.4 samples, respectively. It is reasonable to infer that LNMO-0.2 sample should have the best structural stability, which can be verified by the following cycling performance curves in Fig. 6.

It is well known that the $LiNi_{0.5}Mn_{1.5}O_4$ spinel takes on two distinct space groups according to the ordering of transition

metal cations: the simple cubic $P4_332$ space group with Ni^{2+} and Mn^{4+} ions occupying the 12d and 4b sites, respectively, and the face centered cubic *Fd3m* space group with Ni^{2+} and Mn^{4+} ions randomly distributing on 16d sites.[37,38] XRD characterization cannot distinguish between the two space groups due to the similar scattering factors of Ni and Mn, which can be accomplished by FT-IR spectra. As mentioned by Kunduraci *et al.*,[39] $P4_332$ space group has eight absorption peaks in FT-IR spectrum, while *Fd3m* space group only has five ones, and the intensity ratio of $I(576\ cm^{-1})/I(615\ cm^{-1})$ increases with the cation ordering degree. From Fig. 2 it can be seen that all samples can be classified as *Fd3m* space group. The intensity ratios of $I(576\ cm^{-1})/I(615\ cm^{-1})$ for LNMO-0.1, LNMO-0.2, LNMO-0.3 and LNNO-0.4 samples are 0.930, 0.971, 1.002 and 0.994, respectively, that is, the disordering degree (Mn^{3+} content) initially decreases and then increases slightly with the increase of reactant concentration, in accordance with XRD result.

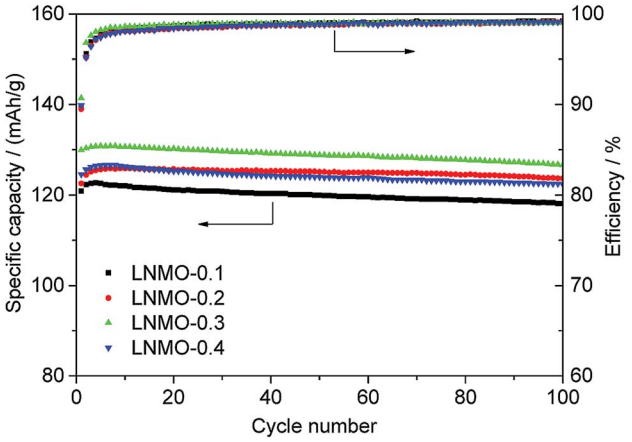

Fig. 6 Cycling performance and coulombic efficiency of $LiNi_{0.5}Mn_{1.5}O_4$ samples synthesized at different reactant concentrations at 1C rate.

Morphology of samples

As is well known, the structure and morphology have great influences on the electrochemical performance of electrode materials for LIB. The SEM images of the carbonate precursors prepared with different reactant concentrations are shown in Fig. 3(a–d). It can be seen that the precursor samples exhibit a gradually decreasing particle size with the increase of reactant concentration. Generally, the growth process of crystals can be separated into two steps, an initial nucleation stage and a subsequent crystal growth process. It is believed that chemical precipitation is a process of competition between crystal nucleation and crystal growth, which has a great relationship with the particle size. The increase of reactant concentration will lead to an increasing nucleation rate, thus leading to the gradual decrease in particle size. However, as for NMC-0.4 sample, there exists some large particles (3–4 μm in diameter) caused by the agglomeration of small particles, leading to its nonuniform particle size distribution. Among the four precursors, NMC-0.3 sample shows the most homogeneous particle size distribution with smaller average particle size of 3 μm. It is generally accepted that both particle size and distribution homogeneity exert an influence on the electrochemical performance of final product, therefore better electrochemical performance of LNMO-0.3 sample can be expected.

In addition, the particle morphology also varies with the reactant concentration. From Fig. 3 we can see that NMC-0.1 sample exhibits shuttle-like morphology, NMC-0.2 and NMC-0.3 samples show peanut-like morphology, or rather, the combination of two spherical particles with each other, and NMC-0.4 sample shows spherical morphology. It can be seen that the sphericity of the particle gradually increases with reactant concentration, in other words, the higher the reactant concentration, the easier it is to form spherical particles, in consistence with the finding of ref. 40. Bai *et al.*[40] synthesized a three-dimensional fusiform hierarchical micro/nano Li-rich $Li_{1.2}Ni_{0.2}Mn_{0.6}O_2$ cathode material through a hydrothermal method followed by heat-treatment process. They suggested that in order to make sure the morphology of material to be non-spherical, the amount of transition metal ion should be low, because higher the concentration of reagent is, easier to make the crystal nucleation grow to be sphere-shape, which is in consistence with this work.

SEM images of the as-prepared $LiNi_{0.5}Mn_{1.5}O_4$ samples are shown in Fig. 3(e–k). It can be seen that the $LiNi_{0.5}Mn_{1.5}O_4$ samples exhibit a good inherited morphology from carbonate precursors, that is, shuttle-like morphology for LNMO-0.1, peanut-like morphology for LNMO-0.2 and LNMO-0.3, as well as spherical morphology for LNMO-0.4. Compared with corresponding carbonate precursor, the $LiNi_{0.5}Mn_{1.5}O_4$ product exhibits a relatively smaller secondary particle size caused by volume shrinkage during calcination and a relatively larger primary particle size resulting from the fusion of subunits, whose surface is much rougher than before calcination with a significant fraction of the particles having cracks. But, by and large, with the increase of reactant concentration, the particle

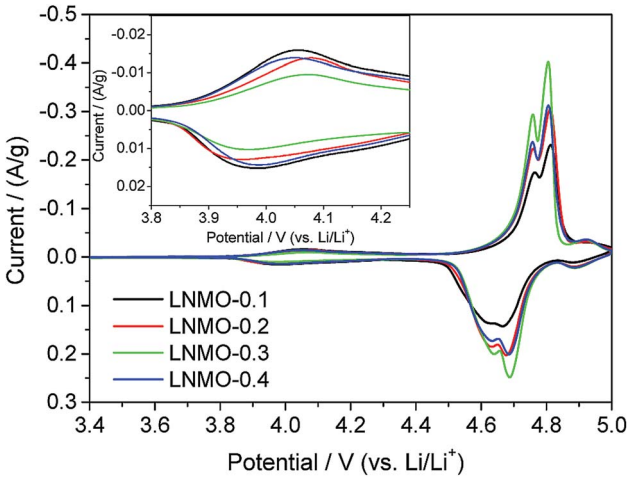

Fig. 5 Cyclic voltammograms of $LiNi_{0.5}Mn_{1.5}O_4$ samples at scan rate of 0.1 mV s^{-1} between 3.4 and 5.0 V.

morphology and size of $LiNi_{0.5}Mn_{1.5}O_4$ product vary in a similar trend of carbonate precursor. Therefore, it is a feasible way to tailor the particle morphology and size of $LiNi_{0.5}Mn_{1.5}O_4$ by tailoring their precursors' morphology and size, which can be controlled by reactant concentration.

The typical broken hollow particles of $LiNi_{0.5}Mn_{1.5}O_4$ samples synthesized at 0.2–0.4 mol L^{-1} reactant concentrations are shown in Fig. 3(i–k), the magnified image of the region marked with a circle in Fig. 3(f–h), and the hollow interior can be clearly observed from the broken part. From the broken particle in Fig. 3(i–k), the wall of $LiNi_{0.5}Mn_{1.5}O_4$ hollow particles is composed of interconnected submicron polyhedral subunits. It is worth noting that the wall thickness of $LiNi_{0.5}Mn_{1.5}O_4$ samples synthesized at 0.2–0.4 mol L^{-1} reactant concentrations is about 0.7, 0.6 and 0.3 μm, respectively, that is, the wall thickness gradually decreases with reactant concentration. It is speculated that the wall of LNMO-0.1 sample is so thick that the hollow structure cannot be observed from Fig. 3(e), and that of partial LNMO-0.4 breaks into small particles due to thinner wall, as shown in Fig. 3(k). The variation of wall thickness can be explained as follows. It has been reported that the particles in the core of carbonate precursor is formed by nucleation process, which have a relatively smaller size and a lower density due to the initial higher supersaturation. However, the wall is formed by gradual crystal growth process, whose compositional particles have a relatively larger size and a higher density.[41] During high-temperature calcination, the carbonate precursor will go through volume shrinkage to obtain $LiNi_{0.5}Mn_{0.5}O_4$ particle. So the core with low density becomes sparse or even disappeared, and the wall with high density is still compact in $LiNi_{0.5}Mn_{0.5}O_4$. The increase of reactant concentration results in the increased nucleation rate, thus leading to the gradual decrease in wall thickness of $LiNi_{0.5}Mn_{1.5}O_4$ product. Wang *et al.*[41] thought that the formation of hollow structure may be caused by Ostwald ripening. Due to the high surface energy of the small crystallites in core compared to the larger ones in wall, the smaller crystallites in the cores transferred to the wall during calcination process. This hollow hierarchical structure can provide a larger surface area and a reduced diffusion distance for both Li^+ ions and electrons, and the internal void space can effectively accommodate the volume change resulting from the repeated Li^+ ion intercalation/deintercalation, which is favourable to electrochemical performance.

To further confirm the hollow hierarchical structure of as-prepared samples, nitrogen adsorption/desorption measurements were performed. Fig. S3† shows the adsorption/desorption isotherms and corresponding BJH pore size distribution plots of the materials. According to IUPAC classification, all isotherms can be attributed to type IV, indicating the presence of mesopores. From the pore size distribution plots it can be seen that there are abundant mesopores ranged from 2 to 20 nm existing in the materials. The loops observed can be ascribed to type H1, corresponding to the particle assembly, in consistence with the particle structure of as-prepared samples. The surface areas obtained according to BET method are 2.386, 3.616, 4.262 and 3.935 $m^2\ g^{-1}$, respectively, for LNMO-0.1, LNMO-0.2, LNMO-0.3 and LNMO-0.4 samples. Using the BJH method and the desorption branch of the nitrogen isotherm, the cumulative pore volumes are 8.09×10^{-3}, 12.80×10^{-3}, 14.95×10^{-3} and 13.96×10^{-3} $cm^3\ g^{-1}$ for LNMO-0.1, LNMO-0.2, LNMO-0.3 and LNMO-0.4 samples, respectively. The relatively larger specific surface area and higher porosity of LNMO-0.3 sample could offer larger electrode/electrolyte contact area and promote Li^+ ion diffusion,[42,43] therefore, better electrochemical performance can be expected.

Electrochemical properties

To evaluate the rate capability, the cells were tested from 0.2C to 10C in the voltage range of 3.5 to 4.95 V and the charge rates were equal to the discharge rates. At each rate, a constant-current charge step was followed by a constant-voltage step until the current decreased to 1/10 of the applied current. Fig. 4(a) displays the charge/discharge curves of as-prepared $LiNi_{0.5}Mn_{1.5}O_4$ samples at rates of 0.2C, 1C, 5C and 10C. All discharge curves show a long plateau at ~4.7 V, arising from Ni^{2+}/Ni^{4+} redox couple, as well as a short plateau at ~4.0 V, associated with Mn^{3+}/Mn^{4+} redox couple. The presence of 4.0 V plateau implies that the as-prepared $LiNi_{0.5}Mn_{1.5}O_4$ samples mainly have disordered structure with *Fd3m* space group, in consistence with FT-IR result. Based on the discharge curves at 0.2C rate, the Mn^{3+} contents can be calculated from the discharge capacity between 3.8 and 4.25 V being divided by the total discharge capacity,[44] which are 12.06%, 11.33%, 9.34% and 10.62%, respectively, for LNMO-0.1, LNMO-0.2, LNMO-0.3 and LNMO-0.4 samples. It can be seen that the Mn^{3+} content first decreases and then increases with the reactant concentration, and LNMO-0.3 sample has the lowest Mn^{3+} content, in consistence with the above XRD and FT-IR results. In addition, with increasing current density, the voltage difference between charge and discharge plateau increases due to the limited Li^+ ion diffusion kinetics, meaning increasing polarization. A smaller voltage difference between charge and discharge plateau indicates better rate capability. Besides, the rate capability can also be evaluated by proportion of constant-current charge step in total charge capacity at large currents.[11] The constant-current charge step contributes 87.3%, 92.0%, 92.1% and 88.8% to the total charge capacity at 5C in LNMO-0.1, LNMO-0.2, LNMO-0.3 and LNMO-0.4, respectively. The above results indicate that LNMO-0.3 sample exhibits the optimal rate capability, whose discharge capacities at 0.2C, 1C, 5C and 10C are 125.0, 128.5, 127.4 and 124.9 mA h g^{-1}, respectively. The discharge capacity at 10C rate accounts for 99.9% of that at 0.2C rate, higher than 99.2% for LNMO-0.1, 98.5% for LNMO-0.2 and 96.3% for LNMO-0.4.

To further evaluate the rate performance of samples, the cells were cycled successively at current densities from 0.2C to 10C, five times at each current density, as shown in Fig. 4(b). Interestingly, the capacities for all electrodes at 1C is higher than 0.2C, which is consistent with the finding of ref. 45. They reported that training at stepwise increasing discharge rates (0.2–1C, up to *ca.* tenth cycle) significantly improved the discharge capacities of the electrodes, probably due to better accessibility of deeper parts of $LiNi_{0.5}Mn_{1.5}O_4$ crystallites and

formation of a solid electrolyte interphase layer on the inner parts. From the figure, we can see that LNMO-0.3 sample exhibits higher discharge capacities at all test rates, manifesting its better rate capability, which can be mainly attributed to its smaller particle size and more homogenous distribution, in spite of lower Mn^{3+} content. In addition, the lower impurity content also contributes to its better rate capability. The worst rate performance of LNMO-0.4 sample may be partly ascribed to the existence of many small particles, because it has been reported that when particles are too small, only a small number of particles can directly contact the conductive additive and many interfaces exist between the particles.[41] It can be concluded that excessive decrease in particle size is unfavorable to rate capability, which is consistent with the finding of ref. 41. In addition, the hollow hierarchical structure with connected primary subunits can facilitate rapid Li^+ ion diffusion and efficient mass-electrolyte contact because of the significantly shortened diffusion route and a large surface-to-volume ratio, which may also be conductive to rate capability.

Fig. 5 shows the cyclic voltammograms of as-prepared $LiNi_{0.5}Mn_{1.5}O_4$ samples between 3.4 and 5.0 V at scan rate of 0.1 mV s^{-1}. For all curves, there appear redox peaks at about 4.0 V corresponding to Mn^{3+}/Mn^{4+} reaction and at about 4.7 V corresponding to Ni^{2+}/Ni^{4+} reaction, in accordance with the charge/discharge curve in Fig. 4(a). This is characteristic of $LiNi_{0.5}Mn_{1.5}O_4$ with *Fd3m* space group.[46,47] It is noteworthy that a minor redox peak appears at around 4.9 V, which is reported to be caused by the electrolyte decomposition.[48] Moreover, it has been reported that $LiNi_{0.5}Mn_{1.5}O_4$ with a disordered structure shows two split peaks at around 4.7 V while that an ordered structure only gives one peak at around 4.7 V,[49] which also confirms the disordered *Fd3m* space group of as-prepared samples, consistent with the FT-IR analysis. From the inset magnified image of 4.0 V peak, it can be seen that the Mn^{3+} content decreases in the order of LNMO-0.1 > LNMO-0.2 > LNMO-0.4 > LNMO-0.3, in consistence with the Mn^{3+} content calculated from initial discharge curves at 0.2C rate in Fig. 4(a).

The voltage differences between anodic (φ_a) and cathodic (φ_c) peaks reflect the polarization degree of the electrode, which is listed in Table S2.† The bigger the potential difference between Li^+ ions intercalation and deintercalation is, the stronger the electrode polarization is. It can be observed that LNMO-0.3 sample exhibits the smallest potential difference (for Ni^{2+}/Ni^{3+} and Ni^{3+}/Ni^{4+}) among all samples, indicating its best reversibility of Li^+ ions during intercalation/deintercalation process, which in turn ensures its optimal rate capability and cycling performance.[50] In addition, the higher peak intensity of LNMO-0.3 sample also confirms its higher specific capacity, in consistence with Fig. 4(a).

Cycling performance is also of significant importance for powering LIB. Fig. 6 shows cycling performance and coulombic efficiency of $LiNi_{0.5}Mn_{1.5}O_4$ materials in the voltage range of 3.5–4.95 V at 1C rate and room temperature. From the initial charge/discharge curves in Fig. S4,† we can get that the initial coulombic efficiencies are 89.7%, 89.5%, 90.7% and 89.9%, respectively, for LNMO-0.1, LNMO-0.2, LNMO-0.3 and LNMO-0.4 samples. The coulombic efficiencies of all four samples are gradually improved in initial several cycles and then stabilized at ~99%. The formation of solid electrolyte interphase (SEI) film results in the relatively low coulombic efficiency during initial cycles, which is of great importance in preventing electrolyte decomposition, thus leading to the stabilization of coulombic efficiency in the following cycles. In consideration of the capacity increase in initial several cycles, the 5^{th} cycle was chosen for relative capacity retention. Based on Fig. 6 we can get that the discharge capacities at 5^{th} cycle and 100^{th} cycle are 122.6/118.1, 125.7/123.7, 130.8/126.6 and 126.5/122.4 mA h g^{-1}, and the corresponding capacity retention rates are 96.3%, 98.4%, 96.8% and 96.8%, respectively, for LNMO-0.1, LNMO-0.2, LNMO-0.3 and LNMO-0.4 samples. It can be seen that LNMO-0.2 sample shows the best cycling performance, which is consistent with its highest I_{311}/I_{400} intensity ratio obtained from XRD pattern.

It has been reported that the factors influencing the cycling performance of $LiNi_{0.5}Mn_{1.5}O_4$ cathode material mainly include the side reactions with electrolyte[51] and Mn dissolution at high voltage,[52,53] as well as the presence of rock-salt impurity phase,[30,33,47] *etc.* The side reaction is closely relevant to the contact area between electrode and electrolyte, and the higher the contact area, the more severe the side reaction with electrolyte. The Mn dissolution mainly results from the disproportionation reaction of Mn^{3+} ($2Mn^{3+} = Mn^{2+} + Mn^{4+}$),[54] that is, the existence of Mn^{3+} in the cathode is the main reason for the Mn dissolution,[55] therefore higher Mn^{3+} content may lead to severe Mn dissolution and severe strain from Jahn–Teller distortion.[3,56,57] In addition, it has been reported that the Mn dissolution of $LiMn_2O_4$ spinel is often accelerated with larger specific surface area,[58,59] which should be also applicable to $LiNi_{0.5}Mn_{1.5}O_4$, a derivative of $LiMn_2O_4$. The impurity phase tends to react with the electrolyte and thus causes capacity fading.[47] Based on above analysis, it can be inferred that the better cycling performance of LNMO-0.2 sample can be attributed to its appropriate particle size, Mn^{3+} content and impurity content. The inferior cycling performance of LNMO-0.1 sample may be attributed to the higher Mn^{3+} and impurity contents, while that of LNMO-0.3 and LNMO-0.4 samples may be mainly ascribed to the smaller particle size.

But then again, the as-prepared $LiNi_{0.5}Mn_{1.5}O_4$ samples with hollow hierarchical structure show superior cycling performance to that of bulk electrode,[31,60–62] which can be mainly attributed to that the small primary particles and interior void space allow for facile penetration by the electrolyte and effectively release the strain caused by the volume change during the repeated Li^+ insertion/extraction cycles.[5,63] The superior structural integrity of hollow structure can also be confirmed by the SEM image of four electrodes after cycling 100 times at 1C rate, as shown in Fig. S5.† The very small particles in the image are conductive additive (acetylene black). Compared with the original SEM images in Fig. 3, all samples can maintain their original morphology after 100 cycles, and the hollow structure of LNMO-0.2, LNMO-0.3 and LNMO-0.4 samples is still visible. It means that the hollow structure of all samples is very stable, which is not broken in the charge/discharge cycling process. Therefore, their excellent cycling performance can be partly

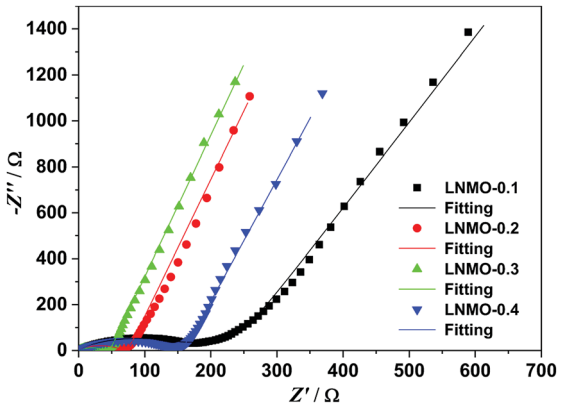

Fig. 7 Nyquist plots for $LiNi_{0.5}Mn_{1.5}O_4$ samples synthesized at different reactant concentrations.

ascribed to buffering effect of the hollow interior during the repeated Li^+ ion insertion/extraction processes. Taking the discharge capacity, rate capability and capacity fading factor into account, LNMO-0.3 sample shows a balance of electrochemical properties, which agrees with the deduction obtained from Fig. 3.

Electrochemical impedance spectroscopy (EIS) is an important technique for evaluating the interfacial electrochemistry as well as the reaction kinetics in LIB materials. Impedance spectra were conducted on the $LiNi_{0.5}Mn_{1.5}O_4$/Li cells to further understand the different electrochemical performances of $LiNi_{0.5}Mn_{1.5}O_4$ samples synthesized at different reactant concentrations. Nyquist plots were obtained in the frequency range from 100 kHz to 10 mHz at full-discharged state after 3 cycles at 1C rate, as shown in Fig. 7. It can be seen that each plot contains a semicircle and an oblique line. The intercept at Z' axis is relative to the ohmic resistance (R_e) of electrolyte. The semicircle at the high-to-medium frequency region is attributed to the impedance (R_f) and constant phase element (CPE-1) of the SEI film, and the charge-transfer impedance (R_{ct}) and constant phase element (CPE-2) of the electrode/electrolyte interface. While the oblique line at the low frequency region can be ascribed to the Warburg impedance (W_0) related to Li^+ ion solid-state diffusion in the electrode.[64] The Nyquist plots were fitted by ZView software based on the equivalent circuit in Fig. S6,† and the fitting lines match with the experimental data very well, as shown in Fig. 7. From the fitting parameters listed in Table S3,† it can be clearly observed that the difference of R_e and R_f between the four electrodes is negligible. Meanwhile, the charge-transfer resistance (R_{ct}) exhibits considerable difference between these four electrodes, which are greatly higher than the resistances of SEI film, indicating that the charge-transfer resistance is a dominant factor of the electrochemical kinetics of electrode. As shown in Table S3,† the charge-transfer resistance is 193.40, 63.47, 38.50 and 143.90 Ω for LNMO-0.1, LNMO-0.2, LNMO-0.3 and LNMO-0.4 samples after 3 cycles at 1C rate, respectively, that is, the charge-transfer resistance first decreases and then increases with the reactant concentration increasing. Among them, LNMO-0.3 sample has the lowest charge-transfer resistance, indicative of the fastest Li-intercalation kinetics. In general, for LIB cathode materials, electronic and ionic conductivity are two key aspects to the charge-transfer resistance. In detail, the materials able to exhibit higher electronic and ionic conductivity possess better rate performances.[65] Therefore, the lower charge-transfer resistance and higher Li^+ ion diffusion coefficient are accountable for the high capacity and excellent rate performance of LNMO-0.3 sample, which can be mainly attributed to the smaller particle size with homogeneous distribution and lowest impurity content, despite a less disordered structure.

The better cycling performance of samples is further supported by the EIS spectra after 100 cycles at 1C rate, which are shown in Fig. S7.† The fitted results obtained by ZView software are shown in Table S3.† It can be seen that both SEI film resistance and charge-transfer resistance are increased after cycling 100 times in comparison with cycling 3 times, and the charge-transfer resistances are 203.50, 77.41, 48.36 and 158.00 Ω, respectively, for LNMO-0.1, LNMO-0.2, LNMO-0.3 and LNMO-0.4 samples. It can be seen that in comparison with the EIS spectra after cycling 3 times (Fig. 7), the R_{ct} values increase slightly, which suggests that the interparticle resistance of the electrode is suppressed by the hollow hierarchical structure. Therefore, the electrons and Li^+ ions can transfer efficiently on the interface of active material and electrolyte, thus resulting in enhanced electrode reaction kinetics and excellent cycling performance of the samples.

In order to determine the Li^+ ion diffusion coefficients (D_{Li^+}), galvanostatic intermittent titration technique (GITT) was carried out for all electrodes. In this experiment, a small current pulse (0.2C) was applied for 10 min and the cell was then allowed to rest at open circuit for 30 min. Fig. S8(a)† shows the GITT curves of as-prepared $LiNi_{0.5}Mn_{1.5}O_4$ samples in the 3rd charge/discharge process. Obviously, LNMO-0.3 samples has smaller polarization than other samples. Fig. S8(b)† shows a typical E *vs.* τ profile at a selected titration for LNMO-0.3 sample. According to the GITT measurement, the chemical diffusion coefficient of Li^+ ion can be calculated by the following eqn (1):[66,67]

$$D_{Li^+} = \frac{4}{\pi}\left(\frac{mV_M}{MA}\right)^2\left(\frac{\Delta E_s}{\tau\left(\frac{dE_\tau}{d\sqrt{\tau}}\right)}\right)^2 \quad \left(\tau \ll \frac{L^2}{D_{Li^+}}\right) \qquad (1)$$

where V_M is the molar volume of samples which is deduced from the crystallographic data, M and m are the molecular weight and the mass of active material. A is the electrode contact area with the electrolyte obtained from the BET surface area, and L is the thickness of the electrode. τ is the constant current pulse time and ΔE_s is the difference between the steady potentials. Since E *vs.* $\tau^{1/2}$ is linear over the entire time period of current flux (Fig. S8(c)†), then eqn (1) can be further simplified as eqn (2):[68,69]

$$D_{Li^+} = \frac{4}{\pi\tau}\left(\frac{mV_M}{MA}\right)^2\left(\frac{\Delta E_s}{\Delta E_\tau}\right)^2 \qquad (2)$$

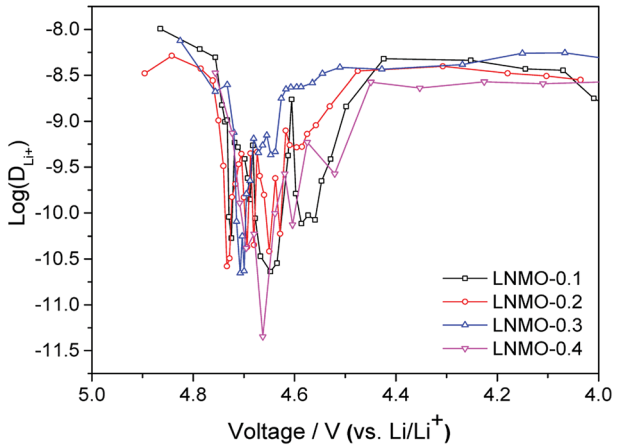

Fig. 8 Li^+ ion diffusion coefficient for all electrodes during 3rd discharge process.

in which, ΔE_τ is the total transient voltage change of the cell for an applied galvanostatic current for the time τ. Based on eqn (2), the obtained D_{Li^+} values at different potentials during the 3rd discharge process are presented in Fig. 8. It can be seen that the diffusion coefficients strongly depend on the potential. There is absence of the constant diffusion coefficients in the two-phase coexisting region around 4.7 V for the material with *Fd3m* space group, where the Li^+ ion diffusivity is slower, in consistence with ref. 70. However, the four samples exhibit similar D_{Li^+} values in the range of 10^{-8} to 10^{-11} cm^2 s^{-1} during the lithium insertion process irrespective of the particle size, higher than those reported in ref. 69–71, which can be attributed to the hollow hierarchical structure of as-prepared samples. Whereas, the relatively small particle size and more homogeneous distribution of LNMO-0.3 sample could shorten the diffusion distance of Li^+ ions, thus leading to its superior rate capability and cycling performance, in consistence with Fig. 4 and 6.

Conclusions

Hollow hierarchical $LiNi_{0.5}Mn_{1.5}O_4$ cathode material has been successfully synthesized *via* a urea-assisted hydrothermal method followed by high-temperature calcination process. The effects of reactant concentration on the structure, morphology and electrochemical properties of carbonate precursor and corresponding $LiNi_{0.5}Mn_{1.5}O_4$ product have been intensively investigated. XRD analysis shows that all four samples belong to cubic spinel structure, and the $LiNi_{0.5}Mn_{1.5}O_4$ sample synthesized at 0.3 mol L^{-1} has the lowest impurity content. FT-IR spectra illustrate that all four samples have mainly the disordered structure with *Fd3m* space group, and the disordering degree (Mn^{3+} content) initially decreases and then increases slightly with the reactant concentration increasing. Among them, the LNMO-0.3 sample has the lowest Mn^{3+} content. SEM observation shows that the average particle size of carbonate precursor exhibits a decreasing trend with the reactant concentration, and the one synthesized at 0.3 mol L^{-1} has relatively smaller particle size with more homogenous distribution. In addition, the particle morphology changes from shuttle to peanut to sphere with the increase of reactant concentration, in other words, the sphericity of the particle gradually increases with the reactant concentration. It can be concluded that the particle morphology and size of $LiNi_{0.5}Mn_{1.5}O_4$ material can be controlled by changing their precursors' morphology and size, which can be controlled by reactant concentration. Taking the discharge capacity, rate capability and capacity fading factor into account, the $LiNi_{0.5}Mn_{1.5}O_4$ sample synthesized at 0.3 mol L^{-1} reactant concentration shows optimal overall electrochemical properties, which can be mainly attributed to smaller particle size with homogeneous distribution and lowest impurity content, despite a less disordered structure. In addition, the excellent electrochemical performance of as-prepared $LiNi_{0.5}Mn_{1.5}O_4$ material can be partly attributed to the peculiar hollow hierarchical structure, which can not only provide extra active sites and short Li^+ ion diffusion path but also buffer the volume changes and relieve the mechanical strain caused by the repeated insertion/extraction of Li^+ ions. On the basis of this work, this facile urea-assisted homogeneous precipitation-hydrothermal preparation of $LiNi_{0.5}Mn_{1.5}O_4$ material with uniform hollow hierarchical architecture will provide an effective and promising strategy for the synthesis of high energy density cathode materials for lithium ion batteries.

Conflicts of interest

There are no conflicts to declare.

Acknowledgements

The authors are grateful to the Key R&D Plan Self-raised Project of Hebei Province (Grant number 16214406) and Technology Innovation Foundation Project for Outstanding Youth of Hebei University of Technology (Grant number 2013009) for the financial support of this work.

References

1 J. M. Tarascon and M. Armand, *Nature*, 2001, **414**, 359.
2 M. Armand and J. M. Tarascon, *Nature*, 2008, **451**, 652.
3 D. Liu, W. Zhu, J. Trottier, C. Gagnon, F. Barray, A. Guerfi, A. Mauger, H. Groult, C. M. Julien, J. B. Goodenough and K. Zaghib, *RSC Adv.*, 2014, **4**, 154.
4 K. Zhang, X. Han, Z. Hu, X. Zhang, Z. Tao and J. Chen, *Chem. Soc. Rev.*, 2015, **44**, 699.
5 J.-H. Kim, N. P. W. Pieczonka and L. Yang, *ChemPhysChem*, 2014, **15**, 1940.
6 X. Zhang, F. Cheng, J. Yang and J. Chen, *Nano Lett.*, 2013, **13**, 2822.
7 M. R. Jo, Y.-I. Kim, Y. Kim, J. S. Chae, K. C. Roh, W.-S. Yoon and Y.-M. Kang, *ChemSusChem*, 2014, **7**, 2248.
8 F. Wu, Z. Wang, Y. Su, Y. Guan, Y. Jin, N. Yan, J. Tian, L. Bao and S. Chen, *J. Power Sources*, 2014, **267**, 337.
9 L. Zhou, K. Zhang, Z. Hu, Z. Tao, L. Mai, Y.-M. Kang, S.-L. Chou and J. Chen, *Adv. Energy Mater.*, 2017, **8**, 1701415.

10 W. W. Wu, H. F. Xiang, G. B. Zhong, W. Su, W. Tang, Y. Zhang, Y. Yu and C. H. Chen, *Electrochim. Acta*, 2014, **119**, 206.
11 Y. Xue, Z.-B. Wang, L.-L. Zheng, F.-D. Yu, B.-S. Liu, Y. Zhang and Y.-X. Zhou, *RSC Adv.*, 2015, **5**, 100730.
12 L. Zhou, D. Zhao and X. W. Lou, *Adv. Mater.*, 2012, **24**, 745.
13 G. Zhang, L. Yu, H. B. Wu, H. E. Hoster and X. W. Lou, *Adv. Mater.*, 2012, **24**, 4609.
14 J. Li, S. Xiong, Y. Liu, Z. Ju and Y. Qian, *Nano Energy*, 2013, **2**, 1249.
15 H. Luo, P. Nie, L. Shen, H. Li, H. Deng, Y. Zhu and X. Zhang, *ChemElectroChem*, 2015, **2**, 127.
16 Z. Wang, L. Zhou and X. W. Lou, *Adv. Mater.*, 2012, **24**, 1903.
17 X. Liu, D. Li, Q. Mo, X. Guo, X. Yang, G. Chen and S. Zhong, *J. Alloys Compd.*, 2014, **609**, 54.
18 C. Zhu and T. Akiyama, *RSC Adv.*, 2014, **4**, 10151.
19 Y. Xiao, Y. Zhu, T. Gao, B. Zhong and X. Guo, *Ionics*, 2017, **23**, 27.
20 W. Luo, *J. Alloys Compd.*, 2015, **636**, 24.
21 D. Lu, L. Yuan, Z. Chen, R. Zeng and Y. Cai, *J. Alloys Compd.*, 2018, **730**, 509.
22 J. Zhang, X. Guo, S. Yao, W. Zhu and X. Qiu, *J. Power Sources*, 2013, **238**, 245.
23 Y. Liu, M. Zhang, Y. Xia, B. Qiu, Z. Liu and X. Li, *J. Power Sources*, 2014, **256**, 66.
24 A. Cao and A. Manthiram, *Phys. Chem. Chem. Phys.*, 2012, **14**, 6724.
25 L. Wang, G. Liu, W. Wu, D. Chen and G. Liang, *J. Mater. Chem. A*, 2015, **3**, 19497.
26 J. Q. Zhao and Y. Wang, *ECS Trans.*, 2014, **61**, 83.
27 D. Luo, S. Fang, Q. Tian, L. Qu, S. Shen, L. Yang and S. Hdirano, *J. Mater. Chem. A*, 2015, **3**, 22026.
28 W.-H. Ryu, S.-J. Lim, W.-K. Kim and H. S. Kwon, *J. Power Sources*, 2014, **257**, 186.
29 A. van Bommel and J. R. Dahn, *Chem. Mater.*, 2009, **21**, 1500.
30 J.-H. Kim, A. Huq, M. Chi, N. P. W. Pieczonka, E. Lee, C. A. Bridges, M. M. Tessema, A. Manthiram, K. A. Persson and B. R. Powell, *Chem. Mater.*, 2014, **26**, 4377.
31 J. Li, D. Lu, Z. Chen, H. Zeng, A. Li and Y. Cai, *Ionics*, 2017, **23**, 2275.
32 Y. Xue, Z. Wang, L. Zheng, F. Yu, B. Lin, Y. Zhang and K. Ke, *Sci. Rep.*, 2015, **5**, 13299.
33 J. Song, D. W. Shin, Y. Lu, C. D. Amos, A. Manthiram and J. B. Goodenough, *Chem. Mater.*, 2012, **24**, 3101.
34 Z. Bai, N. Fan, Z. Ju, C. Sun and Y. Qian, *Mater. Lett.*, 2012, **76**, 124.
35 M. M. Thackeray, *Prog. Solid State Chem.*, 1997, **25**, 1.
36 S. J. Bao, C. M. Li, H. L. Li and J. H. T. Luong, *J. Power Sources*, 2007, **164**, 885.
37 J.-H. Kim, S.-T. Myung, C. S. Yoon, S. G. Kang and Y.-K. Sun, *Chem. Mater.*, 2004, **16**, 906.
38 Y. Idemoto, H. Narai and N. Koura, *J. Power Sources*, 2003, **119–121**, 125.
39 M. Kunduraci, J. F. Al-Sharab and G. G. Amatucci, *Chem. Mater.*, 2006, **18**, 3585.
40 Y. Li, Y. Bai, C. Wu, J. Qian, G. Chen, L. Liu, H. Wang, X. Zhou and F. Wu, *J. Mater. Chem. A*, 2016, **4**, 5942.
41 Y. Xue, Z.-B. Wang, L.-L. Zheng, F.-D. Yu, B.-S. Liu and Y.-X. Zhou, *ChemistrySelect*, 2017, **2**, 4325.
42 P. G. Bruce, B. Scrosati and J.-M. Tarascon, *Angew. Chem., Int. Ed.*, 2008, **47**, 2930.
43 P. Poizot, S. Laruelle, S. Grugeon, L. Dupont and J.-M. Tarascon, *Nature*, 2000, **407**, 496.
44 T. Risthaus, J. Wang, A. Friesen, A. Wilken, D. Berghus, M. Winter and J. Li, *J. Power Sources*, 2015, **293**, 137.
45 A. V. Potapenko, S. I. Chernukhin, I. V. Romanova, K. S. Rabadanov, M. M. Gafurov and S. A. Kirillov, *Electrochim. Acta*, 2014, **134**, 442.
46 Y.-C. Jin, C.-Y. Lin and J.-G. Duh, *Electrochim. Acta*, 2012, **69**, 45.
47 X. Zhang, F. Cheng, K. Zhang, Y. Liang, S. Yang, J. Liang and J. Chen, *RSC Adv.*, 2012, **2**, 5669.
48 Z. Yang, Y. Jiang, J.-H. Kim, Y. Wu, G.-L. Li and Y.-H. Huang, *Electrochim. Acta*, 2014, **117**, 76.
49 G. B. Zhong, Y. Y. Wang, Y. Q. Yu and C. H. Chen, *J. Power Sources*, 2012, **205**, 385.
50 O. A. Shlyakhtin, S.-H. Choi, Y. S. Yoon and Y.-J. Oh, *J. Power Sources*, 2005, **141**, 122.
51 A. Manthiram, K. Chemelewski and E. S. Lee, *Energy Environ. Sci.*, 2014, **7**, 1339.
52 N. M. Asl, J.-H. Kim, N. P. W. Pieczonka, Z. Liu and Y. Kim, *Electrochem. Commun.*, 2013, **32**, 1.
53 J.-H. Kim, N. P. W. Pieczonka, Z. Li, Y. Wu, S. Harris and B. R. Powell, *Electrochim. Acta*, 2013, **90**, 556.
54 W. Liu, J. Liu, K. Chen, S. Ji, Y. Wan, Y. Zhou, D. Xue, P. Hodgson and Y. Li, *Chem.–Eur. J.*, 2014, **20**, 824.
55 C. Zhan, T. Wu, J. Lu and K. Amine, *Energy Environ. Sci.*, 2018, **11**, 243.
56 O. K. Park, Y. Cho, S. Lee, H.-C. Yoo, H.-K. Song and J. Cho, *Energy Environ. Sci.*, 2011, **4**, 1621.
57 N. P. W. Pieczonka, Z. Liu, P. Lu, K. L. Olsen, J. Moote, B. R. Powell and J.-H. Kim, *J. Phys. Chem. C*, 2013, **117**, 15947.
58 D. H. Jang, Y. J. Shin and S. M. Oh, *J. Electrochem. Soc.*, 1996, **143**, 2204.
59 L.-F. Wang, C.-C. Ou, K. A. Striebel and J.-S. Chen, *J. Electrochem. Soc.*, 2003, **150**, A905.
60 L. Wang, D. Chen, J. Wang, G. Liu, W. Wu and G. Liang, *RSC Adv.*, 2015, **5**, 99856.
61 L. Wang, D. Chen, J. Wang, G. Liu, W. Wu and G. Liang, *Powder Technol.*, 2016, **292**, 203.
62 M.-H. Liu, H.-T. Huang, C.-M. Lin, J.-M. Chen and S.-C. Liao, *Electrochim. Acta*, 2014, **120**, 133.
63 Y.-L. Ding, X.-B. Zhao, J. Xie, G.-S. Cao, T.-J. Zhu, H.-M. Yu and C.-Y. Sun, *J. Mater. Chem.*, 2013, **1**, 7077.
64 R. Jin, H. Jiang, Y. Sun, Y. Ma, H. Li and G. Chen, *Chem. Eng. J.*, 2016, **303**, 501.
65 J. Zeng, Y. Cui, D. Qu, Q. Zhang, J. Wu, X. Zhu, Z. Li and X. Zhang, *ACS Appl. Mater. Interfaces*, 2016, **8**, 26082.
66 J. Zheng, W. Shi, M. Gu, J. Xiao, P. Zuo, C. Wang and J.-G. Zhang, *J. Electrochem. Soc.*, 2013, **160**, A2212.
67 H. Li, X. Wei, P. Yang, Y. Ren, S. Wang, Y. Xing and S. Zhang, *Electrochim. Acta*, 2018, **261**, 86.
68 R. Zhao, Z. Yang, J. Liang, D. Lu, C. Liang, X. Guan, A. Gao and H. Chen, *J Alloys Compd*, 2016, **689**, 318.

69 X. Hao and B. M. Bartlett, *J. Electrochem. Soc.*, 2013, **160**, A3162.
70 A. Ito, D. Li, Y. Lee, K. Kobayakawa and Y. Sato, *J. Power Sources*, 2008, **185**, 1429.
71 J.-H. Kim, S.-T. Myung, C. S. Yoon, I.-H. Oh and Y.-K. Sun, *J. Electrochem. Soc.*, 2004, **151**, A1911.